Mechanisms of elastic wave generation by EMAT in ferromagnetic media

Abdellahi Abderahmane, Bastien Clausse, Alain Lhémery, Laurent Daniel

Mechanisms of elastic wave generation by EMAT in ferromagnetic media

Abdellahi Abderahmane[1,2,3*], Bastien Clausse[1,4†], Alain Lhémery[1‡], Laurent Daniel[2,3].

[1] *Université Paris-Saclay, CEA, LIST, Gif-sur-Yvette, F-91192, France*

[3] *Université Paris-Saclay, CentraleSupélec, CNRS, Laboratoire de Génie Électrique et Électronique de Paris, Gif-sur-Yvette, F-91192 France*

[4] *Sorbonne Université, CNRS, Laboratoire de Génie Électrique et Électronique de Paris, Paris, F-75252, France.*

[2] *EXTENDE, Massy, F-91300, France*

ARTICLE INFO

Keywords:

EMAT
Elastic wave generation
Ferromagnetic materials
Electromagnetic force
Magnetic traction
Magnetostriction strain

ABSTRACT

The present paper deals with the problem of elastic wave generation mechanisms (WGMs) by an electromagnetic-acoustic transducer (EMAT) in ferromagnetic materials. The paper seeks to prove that taking into account all the WGMs must be a general rule to quantitatively predict the elastic waves generated by an EMAT in such materials. Existing models of the various physical phenomena involved, namely magnetic and magnetostrictive, electromagnetic, and ultrasonic, are combined to solve the multiphysics wave generation problem. The resulting model shows that WGMs (i.e., electromagnetic force, magnetostrictive strain, and magnetic traction) strongly depend on material properties and EMAT design and excitation. To illustrate this, four magnetic materials (nickel, AISI410, Z20C13, and low carbon steel) with similar elastic but contrasting electromagnetic properties are studied. A given EMAT of fixed excitation and geometry yields WGMs with highly different amplitudes in these materials, with a WGM dominant in one material being negligible in another. Experimental results make it possible to validate the accuracy of certain predictions of the model developed. In summary, the present work shows that considering all WGMs is the general rule when working with ferromagnetic materials. Furthermore, it offers a generic model that can be integrated into various numerical tools to help optimize EMAT design and give reliable data interpretation.

1. Introduction

In ultrasonic non-destructive techniques, piezoelectric transducers, laser-ultrasonic systems, and electromagneto-acoustic transducers (EMAT) are the most widespread means for generating elastic waves in metallic structures. The piezoelectric techniques use piezoelectric ceramic transducers bound to the structure or radiating from a coupling medium (either solid or fluid). These techniques' need for mechanical contact impedes their potential use in numerous applications. Although optical techniques (using a laser source) do not suffer from this drawback, they are difficult to implement, requiring the surface condition of the part to be inspected, which is sometimes very difficult to ensure industrially. The use of EMAT is restricted to the inspection of conductive and/or magnetic materials. They nonetheless compensate for this shortcoming by being non-contact. They are versatile thanks to the flexibility of their design (*i.e.,* one or several coils and one or several magnets). EMAT has been used on nonmagnetic conductive structures (*i.e.,* aluminum) to generate SH0 (the fundamental shear horizontal mode of plate) [1], SH (bulk shear/transverse horizontal wave) [2], longitudinal wave [3,4], Rayleigh waves [5], S0 (the fundamental Lamb-symmetric mode) [6], and A0 (the fundamental Lamb-antisymmetric mode) [7], and on ferromagnetic structures to generate SH [8], S0 [9], and A0 guided waves [10]. By virtue of its nature (*i.e.,* an

* while at Université Paris-Saclay, CEA LIST

† while at Université Paris-Saclay, CEA LIST

‡ corresponding author: alain.lhemery@cea.fr

electromagnetic (EM) source) EMAT can generate a wave in ferromagnetic (FM) materials through three mechanisms: a) Lorentz force (Lf), b) magnetic force, and c) magnetostriction strain. While the first two are indeed forces, the last one is an eigenstrain (like thermal expansion) caused by the magnetic field and can – for convenience – be represented by a fictitious equivalent force term. Though the theory of wave generation by EMAT in nonmagnetic conductive materials – in which only Lf is created – is rather simple and well established (Gaerttner *et. al.* [11]), that, for the case of ferromagnetic (FM) materials is far more complex to establish. Such materials are widely used across various industries. Their ultrasonic characterization – like that of nonmagnetic materials – often requires the transducer to select specific types of waves, which can be done using EMATs (see [1-10]). The fact that wave generation mechanisms for ferromagnetic materials can interact constructively or destructively hinders the ability to select or even generate elastic waves. Several attempts combining distinct theoretical models have been proposed to solve the EMAT wave generation problem in ferromagnetic materials, which led to some contentions in the recent ultrasonic literature. To understand why, it is recalled that various methods exist to model the EM force (the combination of Lorentz and magnetic forces) exerted on a FM object in an EM field. For instance, the equivalent magnetic sources method (see [12,13]), formulates the problem in terms of the interactions of the EM field with equivalent magnetic currents and charges, Kelvin's method (see [14]), in terms of the interactions with magnetic moments, Korteweg-Helmholtz (see [14,15]) and Maxwell stress tensor (Max-ST) methods (see [16,17]) both use the virtual work principle applied to the EM energy. All four formulations give the same global force exerted on the object (see [18]) as the sum of volume and surface terms. However, they yield different force distributions. As a result, some bad practices arose, in which the volume term from one method is combined with the surface term from another method. Such operation in ultrasonic applications – where the generated wave type is governed largely by the distribution of force – led, unescapably, to consequential discrepancies. A detailed discussion on the hazardous nature of this approach is provided by Seher and Nagy [19]. In addition to the theoretical intricacies, practical questions regarding the dominant wave generation mechanism (WGM) were raised. Magnetostriction was the only mechanism considered by Ribichini *et al.* [20], in which the EMAT static and dynamic magnetic fields were perpendicular. Such EMAT was used to generate SH0 in a nickel plate. Another EMAT, for which the static and dynamic magnetic fields were parallel (see [21,22]) was studied. Only Lorentz force (Lf) was considered when such EMAT was used to generate SH0 in steel. In [20,21] the EMAT coil was a single current-carrying wire, and in [22] a rectangular spiral coil. An EMAT with a meander coil was studied by Thompson [23] where, in contrast with previously cited works with parallel static and magnetic fields, Lf was not neglected by the model and was shown to be dominant in comparison to magnetostriction for large static magnetic field. This was observed for three different FM materials. For low static magnetic field, magnetostriction was the dominant mechanism. Whilst agreement between the model and experiment was mostly good, the latter showed tendencies that the model did not predict, and the author suggested a third WGM, that later on [24] was shown to be the magnetic force. Ashigwuike *et al.* [25] considered the two WGMs previously studied but split Lf into two parts (due to dynamic and static magnetic fields). They numerically compared the contributions of these mechanisms as functions of current for ten steel grades. The dynamic Lf was found to be the dominant mechanism at high currents, while the magnetostriction contribution depended strongly on the material. Although EMATs were used to generate various types of waves, only a few works compared the various WGMs to each other and linked them to the type of generated elastic wave(s). Moreover, when comparison took place, magnetic forces (volume and surface) were deemed insignificant to study or overlooked by the authors. While this does not pose a problem in specific configurations – as seen in Thompson [23] – it should not be regarded as the general rule.

The present work aims to propose a unified model for all three mechanisms of electromagnetic-acoustic transduction in ferromagnetic media and to use this model to highlight, through parametric studies, the need to consider all three. Our findings are presented as follows. In Sec.2, the theoretical model of elastic wave generation (WG) by EMAT in FM is derived. The WG problem is solved in four steps. In the first (Sec.2.1), the electromagnetic problem consisting in obtaining eddy currents, magnetization and magnetostriction from radiated EM fields is solved under the assumption of infinitesimal strain hypothesis (ISH). Such a solution incorporates magnetic and magnetostrictive constitutive laws that were either measured or obtained following multi-scale (Daniel *et al.* [26]) or phenomenological (Jiles [27]) approaches into the solver CIVA-ET [28]. In Sec.2.2, elastic WGMs (volume force distributions) are given in terms of quantities obtained in Sec.2.1. Here, we follow the works of Bossavit [17] and Henrotte *et al* [29] to present Maxwell stress tensor method as an adequate tool to formulate EMAT wave generation mechanisms in ferromagnetic materials. Such formulation is carried out under the piezomagnetic behavior hypothesis (PMH). In Sec.2.3, the volume WGMs are converted – for computational purposes – into equivalent surface stress distributions using a previously developed tool by Clausse and Lhémery [30]. In the last step (Sec.2.4), the elastodynamic problem of calculating the elastic wave radiation from the surface stress distributions is solved semi-analytically (based on Lhémery [31]), using the

convolution of the appropriate Green's tensor and equivalent surface stress distributions. Sec. 3 is dedicated to experimental studies to verify the validity of ISH (Sec.3.1) and PMH (Sec. 3.2). In Sec.3.3, measured and simulated radiated field distributions of both longitudinal (L) and transverse (T) waves are compared to validate the overall modelling approach. Finally, in Sec.4, parametric studies are carried out to compare all WGMs generated by a given EMAT in four different FM materials. Each component of each transduction mechanism is treated separately to ease their comparison. In Sec. 4.1 WGMs and their corresponding radiated waves are studied as functions of material properties. Four ferromagnetic materials (*i.e.,* nickel and three grades of steel) are treated. These have similar elastic but contrasting electromagnetic properties. In Sec. 4.2 WGMs, are studied as functions of EMAT excitation (*i.e.,* the current in the coil, and the static magnetic field of the magnet). Sec.5 summarizes the main findings of the paper.

2. The theoretical model of EMAT generation in ferromagnetic media

An EMAT is an EM source made of a coil (or of several coils) and a magnet (or several magnets) that radiates dynamic fields (electric ($\boldsymbol{E}$) and magnetic ($\boldsymbol{H}_d$)) and a static magnetic field ($\boldsymbol{H}_s$). The dynamic source is an alternative current ($\boldsymbol{I}_e$) circulating in the coil(s), and the static source is the magnet(s). $\boldsymbol{E}$ induces eddy currents ($\boldsymbol{J}_e$) in electrically conductive materials. These currents give rise to Lorentz forces in the presence of magnetic fields. $\boldsymbol{H}_d$ and $\boldsymbol{H}_s$ induce a magnetization ($\boldsymbol{M}$) in magnetic materials. As a consequence, magnetic forces are exerted on the material by an EMAT and a magnetostriction strain ($\boldsymbol{\epsilon}^{ms}$) is also induced. Owing to the dynamic nature of $\boldsymbol{E}$ and $\boldsymbol{H}_d$, these forces and strain create local dynamic strain/displacement in the part of the medium near the EMAT, thus radiating elastic waves in the medium. Throughout the present work, the infinitesimal strain hypothesis (ISH) is maintained: the strain associated with the elastic wave is sufficiently small for EM fields to be accurately computed on the undeformed shape of the part. When valid, ISH allows for the decoupling of electromagnetic problems (Steps 1 and 2 in what follows) and the elastodynamic problem (*i.e.,* the wave radiation problem: steps 3 and 4). ISH is almost always accepted in the case of EMAT on conductive nonmagnetic materials since the wave displacement (few nm [32]) is at least three orders of magnitude smaller than the characteristic length of the elastic wave source (given generally by the skin depth (μm)). However, the case of ferromagnetic materials is different as it involves a static initial deformation due to magnetic force and magnetostriction strain (caused by the presence of the magnet). As a result, ISH is checked in the present work in the case of FM materials.

Elastic wave generation in FM materials by EMAT is a multiphysics problem. To solve it, we divided it into four sub-problems, each of them specific to a given physics. Methods of solutions to these problems have already been developed – separately – in the literature, sometimes by one of the authors of the present paper. They are combined and ordered in the present work following four steps (see Fig.1) to reach the solution to the complete wave generation problem (WGP). For conciseness, they are only briefly reported hereafter, with references to their detailed derivations being provided.

2.1. Step 1: Computing $\boldsymbol{J}_e, \boldsymbol{M}$ and $\boldsymbol{\epsilon}^{ms}$

The first step deals with the calculation of induced eddy currents ($\boldsymbol{J}_e$), magnetization ($\boldsymbol{M}$) and magnetostriction strain ($\boldsymbol{\epsilon}^{ms}$) from radiated fields ($\boldsymbol{E}, \boldsymbol{H}_d$ and $\boldsymbol{H}_s$). We start with the simpler case of conductive nonmagnetic materials in which only eddy currents are induced. To compute them, the solver CIVA-ET [28] is used. It operates under ISH and uses analytic solutions for $\boldsymbol{H}_s$, while the finite element method is used for computing $\boldsymbol{E}$ and $\boldsymbol{H}_d$. Both the coil and a region of interest in the test piece are meshed. This region is defined as the volume in which $\boldsymbol{E}$ and $\boldsymbol{H}_d$ are considered nonnegligible. It represents the location of the elastic wave source previously defined. The case of FM materials is more complex and requires the definition of magnetic and magnetostrictive constitutive laws ($\boldsymbol{M}(\boldsymbol{H})$ and $\boldsymbol{\epsilon}^{ms}(\boldsymbol{H})$). These laws can be obtained experimentally or theoretically. In the present work, when not obtained experimentally, they are either assumed linear or obtained using one of the two following models: the simplified multi-scale model (SMSM) by Daniel *et al.* [26] (derived from the full model [34]) and the phenomenological model by Jiles [27]. In their full forms, they model hysteretic and anhysteretic magnetic and magnetostrictive constitutive laws as functions of both applied magnetic field and mechanical stress. Daniel *et al.* model [34] is derived from first principles and treats the magneto-mechanical problem in a bottom-up fashion, starting at the domain scale and working its way– through homogenization schemes – up to the polycrystal scale. It is predictive as it uses only parameters obtained from stress-free measurements to predict behaviors under stress. Conversely, that proposed by Jiles [27] is a macroscopic phenomenological model, requiring parameters obtained from measurements under stress. To prove the premise of the present work (*i.e.,* all WGMs should be included when designing an EMAT), materials need not be under stress, and hysteresis can be neglected. As a result, only stress-free versions of magneto-mechanical models are used. Within this framework, that by Daniel *et.al.* [26] uses the following three material parameters to describe the anhysteretic behavior: the initial magnetic susceptibility (χ^0), and both the magnetization (M_s) and the magnetostriction strain (λ_s) at saturation. That by Jiles. [27] uses five material

parameters: a dimensionless parameter representing the interdomain coupling (α), M_s, a parameter characterizing the shape of the anhysteretic magnetization (a), two parameters fitted on the anhysteretic magnetostriction curve (γ_{11} and γ_{21}). Experimental procedures from which one identifies the parameters of both models are given in [33] and [35], respectively. Expressions of magnetization and magnetostriction strain as functions of $\boldsymbol{H}$ and material parameters are not reported here due to lack of space and are readily found in [26-27]. Expressions of magnetic and magnetostrictive constitutive laws are then incorporated into the solver CIVA-ET [28] to obtain the induced eddy currents ($\boldsymbol{J}_e$), magnetization ($\boldsymbol{M}$) and magnetostriction strain ($\boldsymbol{\epsilon}^{ms}$).

2.2. Step 2: computing $\boldsymbol{f}^{em}, \boldsymbol{f}^{ms}$ and $\boldsymbol{t}^{m}$

Once the quantities ($\boldsymbol{J}_e, \boldsymbol{M}$ and $\boldsymbol{\epsilon}^{ms}$) are computed, they are converted into body forces. The forces in question are the electromagnetic force $\boldsymbol{f}^{em}$ (combination of Lorentz force and the volume magnetic force) the equivalent magnetostriction force $\boldsymbol{f}^{ms}$ and the surface magnetic traction $\boldsymbol{t}^{m}$. All these forces can be represented using the *augmented Maxwell tensor* given below (see Bossavit [17] for detailed derivation) under the assumption that magnetic induction ($\boldsymbol{B} = \mu_0(\boldsymbol{M} + \boldsymbol{H})$) and field ($\boldsymbol{H}$) are collinear:

$$\boldsymbol{\sigma}^{Mx} = \boldsymbol{B} \otimes \boldsymbol{H} + G(\boldsymbol{H})\boldsymbol{I} - \boldsymbol{C}\!:\boldsymbol{\epsilon}^{ms} \tag{1}$$

where $\boldsymbol{H}$ obeys the following Maxwell's equations in matter given by $\nabla \times \boldsymbol{H} = \boldsymbol{J}_e$ and $\nabla \cdot \boldsymbol{H} = -\nabla \cdot \boldsymbol{M}$. The second order tensor $\boldsymbol{B} \otimes \boldsymbol{H}$ is given by $(\boldsymbol{B} \otimes \boldsymbol{H})_{ij} = B_i H_j$ and $\boldsymbol{C}$ is the elastic stiffness tensor. Finally, $G(\boldsymbol{H})$ denotes the Gibbs energy, defined as (see Henrotte *et al.* [29]):

$$G(\boldsymbol{H}) = -\int^{|\boldsymbol{H}|} B(\boldsymbol{h}) \cdot d\boldsymbol{h} \tag{2}$$

In EMAT applications, the magnetic field and, consequently, all quantities dependent on it (magnetization and magnetostriction) can be decomposed into two parts: a static part stemming from the permanent magnet(s) and a dynamic part from the coil(s). In general, $|\boldsymbol{H}_d| \ll |\boldsymbol{H}_s|$ (*i.e.,* the hypothesis of piezomagnetism (PMH)). Under this hypothesis, one can write (using Taylor series expansion to the first order):

$$\boldsymbol{B}(\boldsymbol{H}_s + \boldsymbol{H}_d) = \boldsymbol{B}_s + \left[\frac{\partial \boldsymbol{B}}{\partial \boldsymbol{H}}\right]_{\boldsymbol{H}_s} \cdot \boldsymbol{H}_d \tag{3}$$

$$\boldsymbol{\epsilon}^{ms}(\boldsymbol{H}_s + \boldsymbol{H}_d) = \boldsymbol{\epsilon}_s^{ms} + \left[\frac{\partial \boldsymbol{\epsilon}^{ms}}{\partial \boldsymbol{H}}\right]_{\boldsymbol{H}_s} \cdot \boldsymbol{H}_d \tag{4}$$

$$G(\boldsymbol{H}_s + \boldsymbol{H}_d) = G_s + \left[\left(\frac{\partial G}{\partial \boldsymbol{H}}\right)\right]_{\boldsymbol{H}_s} \cdot \boldsymbol{H}_d \tag{5}$$

where in Eq. (3) (resp Eq. (4)) the quantity in brackets is the static differential magnetic permeability $\boldsymbol{\mu}_s$ (resp the magnetostrictive coupling tensor $\boldsymbol{d}^{ms}$). Recalling that $\boldsymbol{B}_s \parallel \boldsymbol{H}_s$, one can readily show that $\left[{}^{\partial G}/_{\partial \boldsymbol{H}}\right]_{\boldsymbol{H}_s} = \boldsymbol{B}_s$

Substituting Eq. (3), (4) and (5) into Eq. (1) yields three terms: (a) a static term (b) a term that depends on the product of $\boldsymbol{B}_s \cdot \boldsymbol{H}_d$ and (c) a term of higher orders in $\boldsymbol{H}_d$. Owing to its nature, the static term does not generate waves. The one with higher orders of $\boldsymbol{H}_d$ is disregarded due to its relatively small amplitude (under PMH), so only the second term is of interest in the present work. The divergence of this term gives $\boldsymbol{f}^{em} + \boldsymbol{f}^{ms}$ and the jump of its magnetic part (*i.e.,* without $-\boldsymbol{C}\!:\boldsymbol{\epsilon}^{ms}$) across the interface ($\Gamma$) of two media with different magnetic permeabilities gives $\boldsymbol{t}^{m}$. These expressions are given by:

$$\boldsymbol{f}^{em} = \nabla \cdot (\boldsymbol{B}_s \otimes \boldsymbol{H}_d + \boldsymbol{\mu}_s \boldsymbol{H}_d \otimes \boldsymbol{H}_s - (\boldsymbol{B}_s \cdot \boldsymbol{H}_d)\boldsymbol{I}) \tag{6}$$

$$\boldsymbol{f}^{ms} = -\nabla \cdot \left(\boldsymbol{C}\!:(\boldsymbol{d}^{ms} \cdot \boldsymbol{H}_d)\right) \tag{7}$$

$$\boldsymbol{t}^{m} = [\boldsymbol{B}_s \otimes \boldsymbol{H}_d + \boldsymbol{\mu}_s \boldsymbol{H}_d \otimes \boldsymbol{H}_s - (\boldsymbol{B}_s \cdot \boldsymbol{H}_d)\boldsymbol{I}]_{\Gamma} \tag{8}$$

These force densities are the EMAT elastic wave generation mechanisms (WGMs) in ferromagnetic media under the assumption of piezomagnetic behavior and collinearity of $\boldsymbol{B}$ and $\boldsymbol{H}$. As $\boldsymbol{H}_d$ is a common factor in all three WGMs, wave sources are mostly located near the surface (within ten skin depths) where the EMAT operates. This observation allows for important simplifications, as shown in the next step.

2.3. Step 3: Converting $\boldsymbol{f}^{em}$ and $\boldsymbol{f}^{ms}$ into equivalent surface stresses.

Apart from the surface magnetic traction, the two other source terms are distributed over a volume. An intermediate step in the overall model consists of converting body force into equivalent surface stress distribution. It is introduced to lighten the computational burden. Details of the method allowing such conversion are provided in [33] for planar and in [30] for arbitrary surfaces. The method assumes the volume force distribution to be confined near the surface so that the elastic wavelength should be larger than the force distribution dimension in the piece thickness. Such an assumption is almost always valid in the case of EMAT in ferromagnetic media since the force distribution dimension in the thickness is governed by $\boldsymbol{H}_d$ which does not penetrate such media more than a few skin depths. Given typical frequencies in EMAT applications, the magnetic permeability, and elastic properties of ferromagnetic media, the elastic wavelength is at least two orders of magnitude larger than the skin depth. By using a Taylor series expansion to the second order of the radiation integral of a body force distribution (given in Eq.9), the method [30] makes it possible to rewrite the volume integrals in the form of a surface integral over an equivalent stress distribution (Eq.10). The full derivation [30, 33] was proposed under the assumption of an

elastically isotropic material, but the anisotropic case can be treated the same way (see [36]). We have:

$$\forall \boldsymbol{x} \in \Omega, u_k(\boldsymbol{x}) = \int_{\boldsymbol{x_0} \in \Omega_\delta} \boldsymbol{G}_k(\boldsymbol{x}, \boldsymbol{x_0}) \cdot \boldsymbol{f}(\boldsymbol{x_0}) d\Omega_\delta \quad (9)$$

$$\forall \boldsymbol{x} \in \Omega, u_k(\boldsymbol{x}) \approx \int_{\boldsymbol{X_0} \in \partial\Omega_\delta} \boldsymbol{G}_k(\boldsymbol{x}, \boldsymbol{X_0}) \cdot \tilde{\boldsymbol{\sigma}}_{\boldsymbol{f}}(\boldsymbol{X_0}) d\Gamma \quad (10)$$

Where u, Ω, Ω_δ and $\partial\Omega_\delta$ denote respectively, the displacement field, the test piece volume, the volume in which the force distribution ($\boldsymbol{f}$) is nonnegligible and its surface. The depth of Ω_δ is given by a few skin depths. u_k (resp. $\boldsymbol{G}_k$) is the k-th component of the displacement field (resp. row of Green's tensor). Expressions of the equivalent surface stress distributions $\tilde{\boldsymbol{\sigma}}_{\boldsymbol{f}}$ as functions of moments of $\boldsymbol{f}$ and elastic constants are cumbersome and are provided in [30,33].

Applying this conversion procedure to both $\boldsymbol{f}^{em}$ and $\boldsymbol{f}^{ms}$ yields two equivalent surface distributions $\boldsymbol{\sigma}^{em}$ and $\boldsymbol{\sigma}^{ms}$.The total surface distribution is finally given as the sum of three terms of surface stress as $\boldsymbol{\sigma}^{tot} = \boldsymbol{\sigma}^{em} + \boldsymbol{\sigma}^{ms} + \boldsymbol{t}^{m}$.

2.4. Step 4: computing radiated elastic wave(s) $\boldsymbol{u}$

Once $\boldsymbol{\sigma}^{tot}$ (*i.e.,* the wave source) has been obtained, the elastodynamic wave radiation problem written as

$$(\Omega)\ \nabla \cdot \boldsymbol{\sigma} = \rho \frac{\partial^2 \boldsymbol{u}}{\partial t^2} \quad (11)$$

$$(\partial\Omega_\delta)\ \boldsymbol{\sigma} \cdot \boldsymbol{n} = \boldsymbol{\sigma}^{tot} \quad (12)$$

can be solved – under the infinitesimal strain hypothesis – like any other classical wave radiation problem. To this end, CIVA-UT [28] is used. For illustration, the present work is limited to bulk waves (longitudinal (L) and shear (S)) radiation in elastically isotropic and homogeneous materials. Radiation by a finite-size source (*i.e.,* $\boldsymbol{\sigma}^{tot}$) is solved semi-analytically using the convolution between Green's tensor (the solution for a point source) and the surface distribution $\boldsymbol{\sigma}^{tot}$ (see Lhémery [31] for details).

To summarize, the solution of the problem of elastic wave generation by EMAT in FM materials starts with obtaining magnetic and magnetostrictive constitutive laws, which, when introduced into a specific EM solver, give induced eddy currents, magnetization, and magnetostriction strain. These latter quantities are used by Maxwell-tensor method to give body force distributions, which in turn are converted into equivalent surface stress distributions – to lighten the computational burden – using a convenient method. Finally, this surface distribution represents the source term in a problem of elastic wave radiation.

The methods used in the various steps for solving the overall problem of transduction by EMAT in ferromagnetic media have already been validated separately. In the present work, two fundamental hypotheses (ISH and PMH) are made. Elements of their experimental validation are given in the next section to strengthen the proposed overall solution.

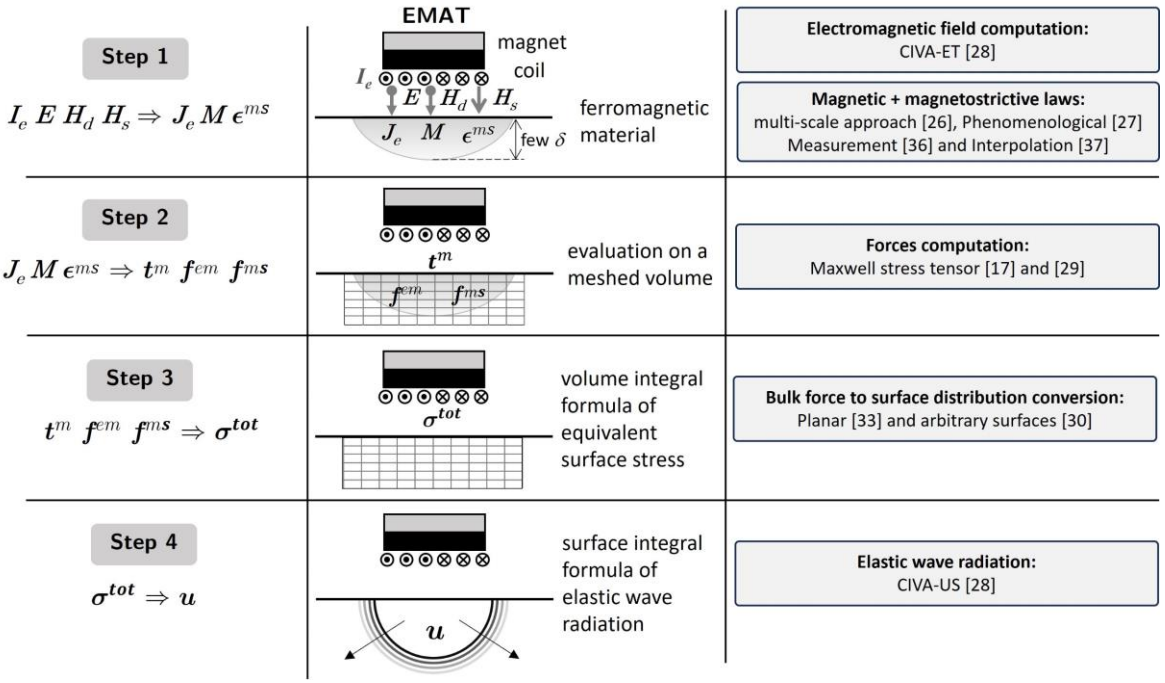

Fig. 1. Schematic representation of the four-step solution of the problem of EMAT generation of elastic wave in ferromagnetic materials. Where the inputs, ouputs methods and models of each step alongside their corresponding references are recalled. 1: Computing induced eddy currents, magnetization, and magnetostriction strain. 2: Computing bulk forces distributions. 3: Converting bulk force distributions to surface force distribution. 4: Computing radiated elastic waves.

3. Experimental validations

The first two subsections of this section treat the validity of infinitesimal strain and piezomagnetic hypotheses. The third presents some experimental validation of the overall model. Obviously, fully validating a multiphysics model as that presented herein is not conceivable, considering the number of parameters involved and their possible interdependence. In what follows, the EMAT used (see Fig.2) is composed of three parts: (a) a circular spiral copper coil (electric conductivity 60 MS/m) of 13 turns, $45\ mm$ outer diameter, $3\ mm$ inner diameter, and $0.34\ mm^2$ wire section (b) two NdFeB (electric conductivity 106 S/m) cylindrical magnets of diameter $50\ mm$, each of 6-mm-height and of normal magnetic induction $1.33\ \mathrm{T}$ (at the center) and (c) a cylindrical steel block (properties given in Table.1) of diameter $50\ mm$ and height $45\ mm$. It was observed experimentally and shown through simulation that using the cylindrical block increased the amplitude of the generated wave as a result of the overall increase in the radiated magnetic field magnitude.

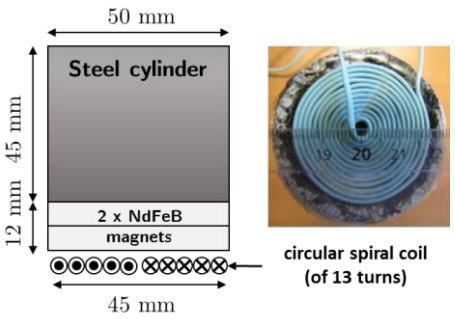

Fig. 2. The EMAT is composed of a circular spiral coil, two NdFeB cylindrical magnets, and a cylindrical steel block.

3.1. Infinitesimal strain hypothesis (ISH)

The EMAT induces both static and dynamic phenomena in FM materials. The former stems from the magnet that exerts a magnetic force and induces a magnetostriction strain in the material. The latter results from the EM fields radiated by the coil. Their magnitudes depend on material properties (elastic, magnetic, and magnetostrictive) and on electrical excitation. The ISH (needed in the development of the solution for the wave generation problem) assumes such deformations to be sufficiently small for the computation of EM fields on the undeformed shape – of the test piece – to give accurate results. Because induced EM fields in materials are not measured directly, we compare measured and computed (by CIVA-ET) *induced electromotive forces* (EMF) to validate ISH. Two configurations are studied, in both, the experimental setup is identical to that in Fig.5 (without the water tank and PZT sensor). In the first (resp. the second) the EMAT is placed above a steel (resp. aluminum) test piece at a distance of $4\ mm$. In both cases, the current in the coil is a pulse of 2 MHz center frequency shown on Fig.3a. A small 2-turn coil (of section $23.8\ mm^2$) is used to measure the induced EMF, from which the electromagnetic induction $\boldsymbol{B}_d$ is deduced. This coil is placed between the EMAT and the test piece and can be moved horizontally (*i.e.,* parallel to the coil plane). A Rogowski coil is also used to measure the current in the EMAT coil, this signal being used in CIVA-ET to compute EM fields. Results from this experiment are given in Fig.3.b (for steel) and Fig.3.c (for aluminum). The material properties of each test piece are given in Table 1. All measurements are made by moving the 2-turn coil along the EMAT coil diameter and maintaining its distance from the test piece at $1.5\ mm$. $B_d(t)$ signal (not shown) is similar to that of current (Fig.3a). Figures 3.b and 3.c show the results for $\underbrace{max}_{t}\ |B_d(t)|$ at each position.

Table 1. EM properties for the two test pieces.

Test piece	Steel	Aluminum
Electric conductivity (MS/m)	11.2	35
Relative magnetic permeability	100	1

Maximum values correspond to EMAT coil center, while null values correspond to its edges, where the magnetic field is predominantly horizontal. Beyond the edges, the normal component of the magnetic field is again predominant. A little further from the coil, EM fields vanish. The very good agreement between measured and simulated signals (assuming ISH) proves the ISH to be valid in this configuration. As a result, both problems – of electromagnetic nature – treated in step 1 and 2 can be dealt with separately from the problems – of elastodynamic nature – treated in step 3 and 4. Such separation allows the use of two different *specialized* numerical solvers (*i.e.,* CIVA-ET and CIVA-UT).

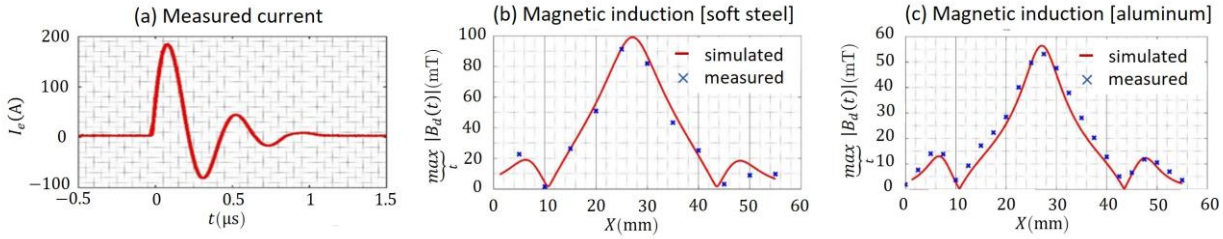

Fig.3. (a) current circulating in the EMAT coil. (b) (resp (c)) comparison of measured and simulated EM induction for different spatial positions along the diameter of the coil (centered at $x = 27.5$ mm, y = 0 mm and z = 4 mm), the sensor is at $z = 1.5\,mm$ of the steel (resp. aluminum) sample surface.

3.2. Piezomagnetic hypothesis (PMH)

EMAT induces static (due to the magnet) and dynamic (due to the coil) magnetic fields in FM materials. The PMH assumes the latter to be sufficiently smaller than the former so that the dynamic problem can be treated as a perturbation of the static one. To validate the PMH, we take the example of a test piece (a cylinder of 70 mm diameter and 147 mm height) made of Z20C13 stainless steel. Measured anhysteretic magnetization and magnetostriction curves are given in Fig.4. To avoid issues stemming from EMAT wave detection and to concentrate on wave generation, a focused piezoelectric transducer (PZT) from Olympus Panametrics of 5.5cm focal length and 2MHz central frequency is used for detection. A calibration experiment whose results are not shown helped identify the current range for which the EMAT generates detectable signals. Although sensitive only to the normal displacement component, the focused PZT can detect shear waves due to their oblique incidence. In other words, due to the size of the sample, the S-wavefront is still spherical when it reaches the bottom surface. It has, therefore a normal component which can be detected by the sensor. The experiment is schematized in Fig.5. The EMAT, the test piece and the PZT are of cylindrical shape and are axisymmetrical relatively to the same axis. The distance between the PZT and the bottom surface of the test piece is maintained at 50mm (equal to the PZT focal distance). The lower half of the test piece and the PZT are immersed in a water tank. A Rogowski coil is used to measure the current I_e (5 cycles of 1 MHz) from the signal generator to the EMAT coil. The lift-off is maintained at 4 mm. Such configuration generates both longitudinal (L) and shear (S) bulk waves in FM materials.

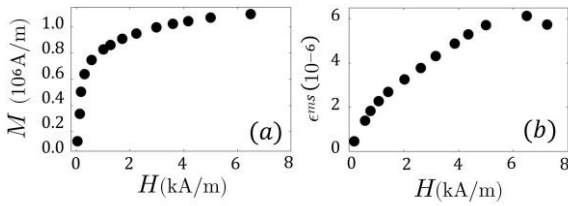

Fig.4. Measured magnetization (a), and magnetostriction (b) as functions of the magnetic field for Z20C13.

To reduce noise, measured signals were averaged over 256 shots. Throughout the present document, longitudinal and shear waves were separated experimentally using their time-of-flight while the simulation tool for field computation (CIVA) is semi-analytical and modal, thus, gives access to their respective fields separately. It is worth noting that in order to compare the signal shapes, all signals were normalized, and measured signals were time-shifted. This allowed superimposing simulated and measured results. The good agreement (Fig.6. (a), (b), (c) and (d)) indicates that no harmonics were generated, which only happens if the PMH is valid. Note that the relatively larger amplitude of the second peak in Fig.d is most likely due to numerical reasons.

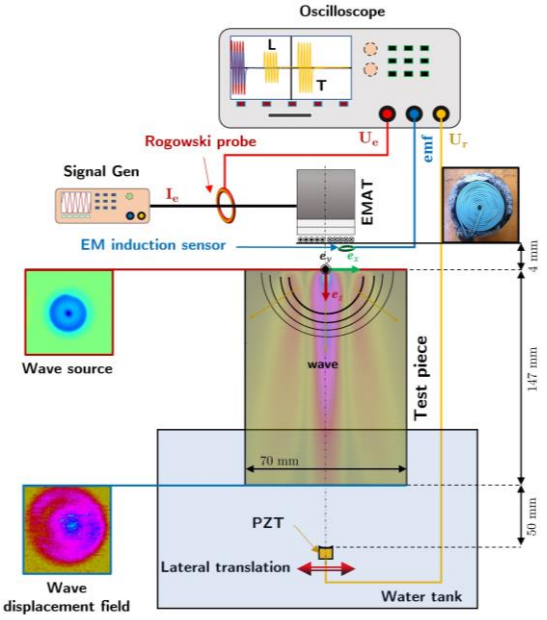

Fig.5. EMAT is placed above the test piece. The current from the signal generator to the EMAT coil is measured by a Rogowski coil. A focused PZT placed beneath the test piece is used for wave detection.

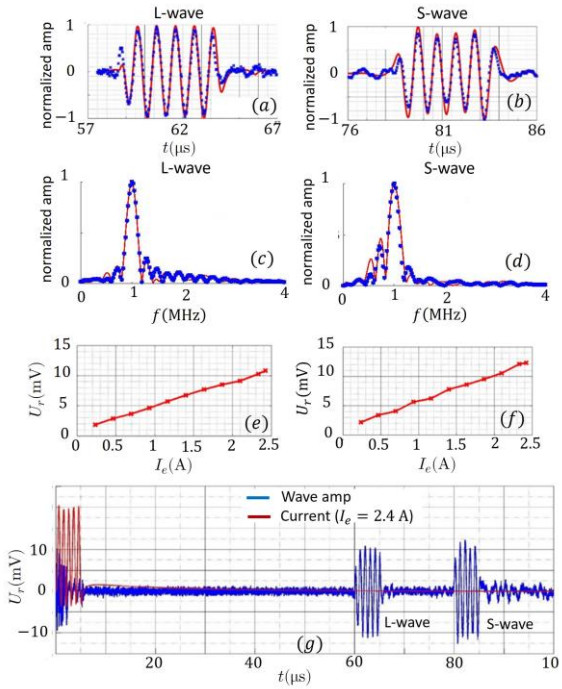

Fig.6. (a) and (b): comparison of measured (blue marker) and simulated (red solid line) time signals for both L and S bulk waves for I = 2.42A. (c) and (d): the Fourier transform of the time signals. (e) and (f): the maximum (measured) amplitude of L and S waves as function of current. (g): measured electric current in the excitation coil and the voltage in the PZT sensor.

To further consolidate this, the maximum amplitudes of measured signals for both L and S waves as functions of I_e are given in Fig.6 (e) and (f). One notices a linear relationship between wave amplitudes and I_e. The latter is proportional to H_d (Maxwell-Ampère) in consequence, a similar linear relationship must also exist between H_d and wave generation mechanisms, which is exactly what PMH predicts (see Eq.6-8). Finally Fig.6g gives the time signal of the excitation current and measured voltages by the PZT sensor. The observed DC offset in current is due to the excitation systems, it doesn't however effect the validity of the hypothesis. In conclusion, these results suggest that higher orders of H_d that would lead to a nonlinear relationship between current and elastic wave amplitudes and would distort the time signal are negligible, thereby consolidating the validity of PMH.

3.3. L and S generation and radiation in FM materials

Now that both the ISH and PMH are verified, one can study the ultrasonic field associated with bulk waves of both polarities radiated by EMAT. For this, the experimental setup is the same as in the previous subsection, with the difference that here I_e is maintained at 2.42 A and the PZT is moved to scan the bottom surface of the test piece. Regarding the simulation, both nonlinear (given in Fig.4a) and linear (given by the slope at the origin of curve in Fig.4a) magnetic constitutive laws were used. Measured (resp simulated) C-scans (maximum amplitude of the wave displacement field at each scanning position) for both L and S waves are presented in Fig.7 (a) and (b) (resp Fig.7 (c) and (d)). A comparison of simulated and measured results along the test piece diameter is given in Fig.7 (e) and (f). All results are normalized using their respective S wave amplitude at the center of the test piece.

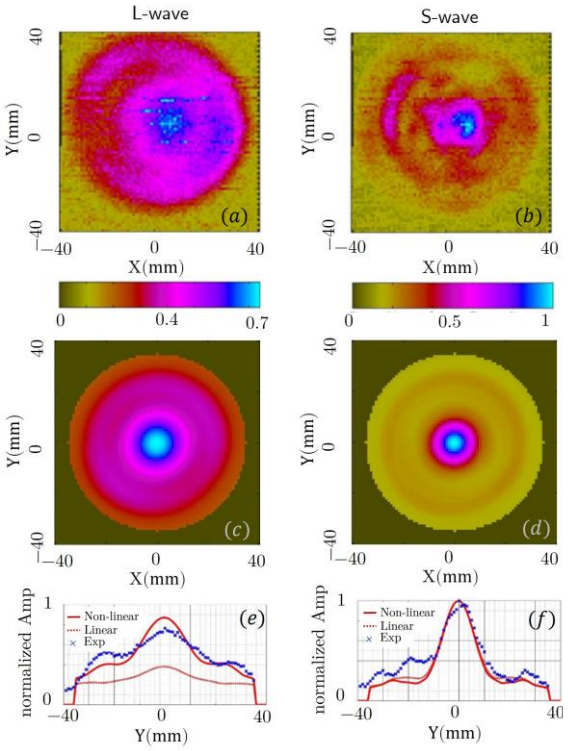

Fig.7. (a) and (b) (resp (c) and (d)): experimental (resp simulated) C-scans for L-wave and S-wave. (e) and (f): comparison of measured (blue markers) and simulated field amplitudes using nonlinear (solid red line) and linear (dotted red line) magnetic constitutive laws.

The dissymmetry in experimental measurements comes from that of the coil. The return wire starts from the coil center and crosses its section: this causes it to tilt (see Fig.5), thereby breaking the symmetry. This is evidenced by the slight shift (to the right) of the central blue spot. Secondary lobes around $\pm 27\,mm$ are also present in the measurements. These are not predicted by simulation using linear magnetic constitutive laws but are predicted when using nonlinear laws. Moreover, the former simulation underestimates the L wave amplitudes along the diameter, contrary to the latter.

4. Parametric studies on EMAT wave generation mechanisms

As stated in Sec.2 EMAT generates waves through three mechanisms: Lorentz force, magnetic force (both volume and surface), and magnetostriction strain. Whilst this is well established in the literature (Thompson [24]), no work, to the best of our knowledge, has considered all three mechanisms together, and no studies were carried out to compare these mechanisms to each other, in different configurations. Such comparison offers important information that should be considered in designing EMAT and interpreting measurements made in ferromagnetic media.

Due to the prohibitive number of inputs in an EMAT experiment (shapes of the coil(s) and magnet(s), current

intensity and frequency, lift-off, material properties, ...), it is extremely difficult to rely solely on the experiment to carry out parametric studies. Conversely, simulation offers both the speed and flexibility required to do so. The present section is divided as follows: In Sec. 4.1 WGMs and their corresponding radiated waves are studied as functions of material properties. In Sec. 4.2 they are studied as functions of EMAT excitation (*i.e.,* the current in the coil and the static magnetic field of the magnet).

4.1. WGMs as functions of material properties

Four materials (nickel, Z20C13, AISI410, and low carbon steel (LCS)) of similar elastic but contrasting electromagnetic properties are studied. Magnetic constitutive laws ($\boldsymbol{M}(\boldsymbol{H})$) are assumed linear. This assumption – not the most suitable to accurately describe experimental data in some cases (see Fig.7) – allows for consequential computational simplification, which is needed to carry out parametric studies. Moreover, nonlinearity is not required to prove the premise of the paper (*i.e.,* all WGMs should be included when designing an EMAT). In both subsections, magnetostrictive constitutive laws are obtained from various approaches. SMSM [26] was used for the anhysteretic curve of nickel. It is measured for that of Z20C13 [37]. The phenomenological approach [27] was used to that of AISI410. Finally, the curve of LCS was obtained by interpolating the corresponding curve appearing in Hirao and Ogi [38]. These curves are shown in Fig.8. Throughout this subsection, current intensity and frequency are $I_e = 0.1$ A, and $f = 1$ MHz, and the normal magnetic induction of the magnet at its center is $B_z = 1.5$ T. Sec.4.1.1 treats WGMs and Sec.4.1.2 their corresponding radiated waves.

Table 2. Material properties for the four FM materials.

Material	ρ (g/cm^3)	C_L (m/s)	C_T (m/s)	σ_e (MS/m)	μ_i
LCS	7.8	5900	3230	1.39	2
Z20C13	7.89	5790	3100	2	15
AISI410	7.67	5590	3000	2	10
Nickel	8.88	5630	2960	15.4	110

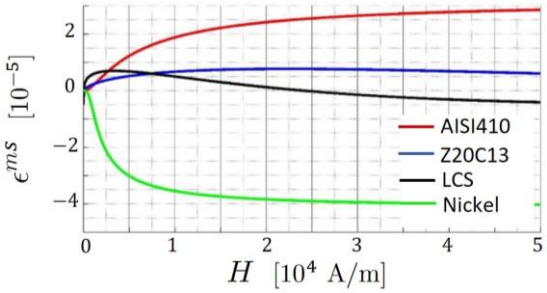

Fig.8. Anhysteretic magnetostrictive curves for nickel, low carbon steel, Z20C13 and AISI410.

4.1.1. $\boldsymbol{\sigma}^{em}, \boldsymbol{\sigma}^{ms}, \boldsymbol{t}^{m}$ *and* $\boldsymbol{\sigma}^{tot}$

The present EMAT would yield in nonmagnetic materials (where only Lorentz force (Lf) is present) a density distribution with a predominant tangential component. To illustrate this, the spatial distribution of WGMs given as equivalent surface stress distributions for LCS (the material with the weakest magnetic and magnetostrictive properties) are shown in Fig.9. The first column relates to the electromagnetic force, the second to magnetostriction, the third, to magnetic traction and the last represents the sum of all previous stress distributions. For a comprehensive illustration, each component is normalized using $\max\left(\max(\sigma_x^{tot}), \max(\sigma_y^{tot}), \max(\sigma_z^{tot})\right)$. A global look at LCS results shows – as expected – a little contribution to the total distribution ($\boldsymbol{\sigma}^{tot}$) from magnetostriction and magnetic traction. As for the electromagnetic force, one can observe the dominance of tangential component, primarily due to Lorentz force (Lf). The magnetic nature of LCS is evidenced by the nonnegligible normal component σ_z^{em}, due to bulk magnetic force. We note that the ability to link tangential components of $\boldsymbol{\sigma}^{em}$ to Lf, and σ_z^{em} to bulk magnetic force stems from the fact that both coil and magnet have a predominant normal magnetic component. This material shows a case in which the predominant WGMs is the Lf. We note that it is nonetheless a mistake to consider only such force in this case since the magnetic bulk force, however small it may be, generates longitudinal waves that are almost not generated by tangential Lf (only by "edge diffraction" which would be nonnegligible only if the source distribution showed a sharp discontinuity (Lhémery [39])).

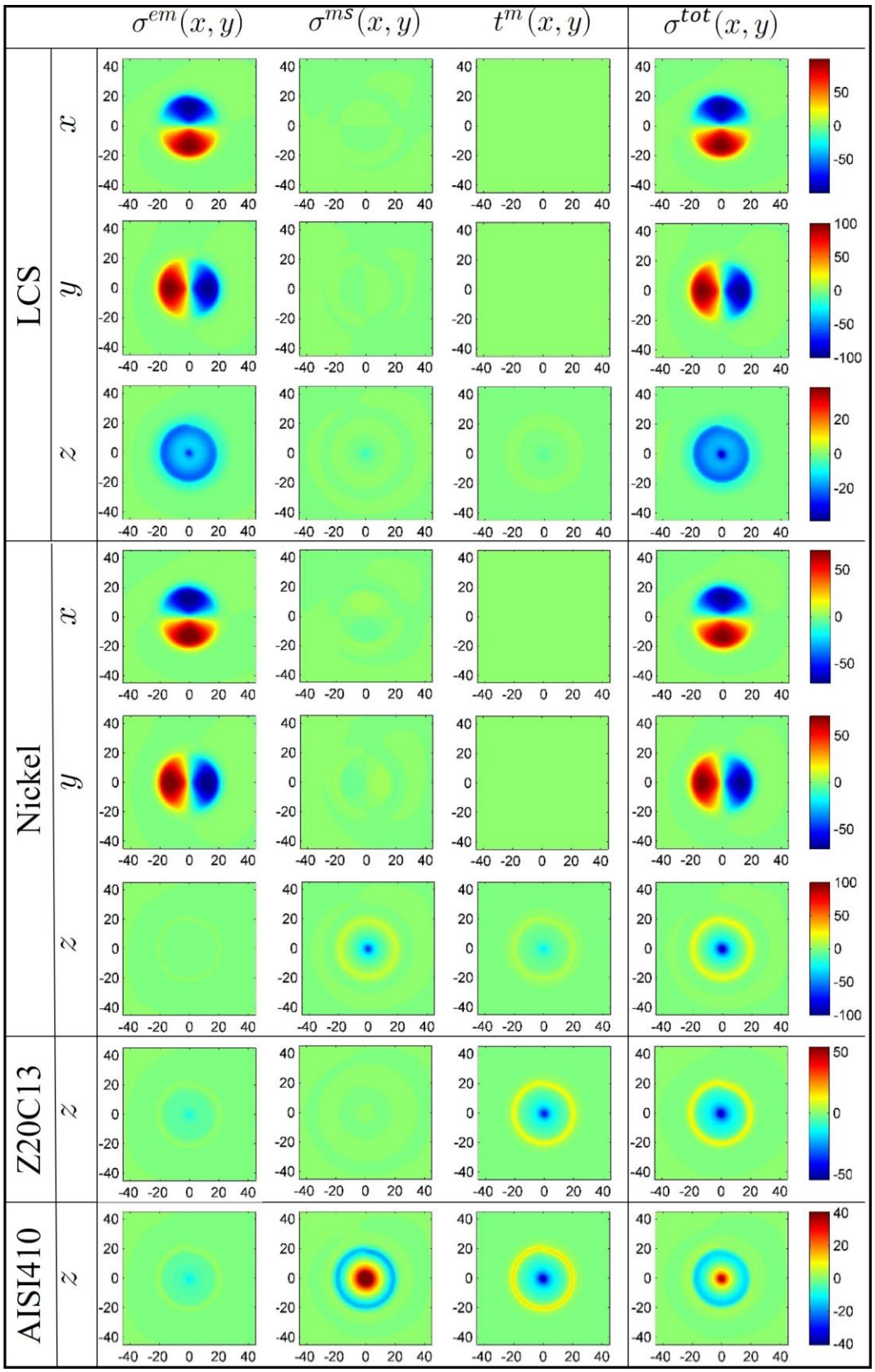

Fig.9. The three wave generation mechanisms for the four studied materials. (For each material) First column: electromagnetic force, second: magnetostriction equivalent force, third: magnetic traction and in the last: total force distribution. For a comprehensive illustration, each component is normalized using $\max\left(\max(\sigma_x^{tot}), \max\left(\sigma_y^{tot}\right), \max(\sigma_z^{tot})\right)$.

This point is discussed in more details in Sec.4.1.2. Consider now the case of nickel (see Fig.9). This material has the strongest electric, magnetic, and magnetostrictive properties amongst the four studied materials. Expectedly

– from the EMAT geometry – tangential components of magnetic traction and magnetostriction are small compared to the electromagnetic force. Looking at $\boldsymbol{\sigma}^{em}$, one can see that the contribution of bulk magnetic force (which is primarily represented by σ_z^{em}) is small compared to that of Lorentz force (represented by $\sigma_{x,y}^{em}$). At first glance, this seems in contradiction to the fact that this material has the highest magnetic permeability. Actually, high permeability means, on the one hand, a high magnetic traction (as seen in the figure) but also a small skin depth, which in turn reduces the volume in which the *bulk* magnetic force operates. The small skin depth also affects Lorentz's force, which, in the present case, is slightly smaller than the equivalent force due to magnetostriction. The large value of the latter force is attributed to its relatively large magnetostriction strain (Fig.8). The example of nickel shows a case in which Lorentz force is no longer the dominant mechanism, and in contrast to the previous case, the normal component of the wave source (σ_z^{tot}) is mainly due to magnetostriction and magnetic traction (instead of the magnetic bulk force for LCS).

EMAT geometry and previous results (for LCS and nickel) suggest that magnetic and magnetostrictive properties manifest themselves mostly through the normal component of WGMs. On this account, for the last two materials (AISI 410 and Z20C13), only normal components are shown (in Fig.9), tangential components being dominated by Lorentz force. Unsurprisingly, the magnetic bulk force for both materials is relatively small due to the relatively higher permeability. As for the contribution to the normal component of the wave source ($\boldsymbol{\sigma}^{tot}$), one sees that it is dominated by magnetic traction for Z20C13 (due to its relatively weak magnetostriction) and is almost evenly distributed between magnetostriction and magnetic traction for AISI410.

The unexpected negative magnetic traction stems from the dynamic problem (wave generation) being treated as a perturbation of the static one (with a given static magnetic traction). Therefore, when $\boldsymbol{H}_d$ opposes $\boldsymbol{H}_s$, the material is *less* pulled towards the magnet, which translates into a traction smaller than that in the static (reference) problem, leading to a negative difference. This also applies to magnetostriction strain. Finally, the observed irregularity in the rotundity of the z-components is caused by the non-axisymmmetric shape of the spiral coil.

In conclusion, an EMAT with a fixed excitation and geometry, would yield in different materials, WGMs with contrasting magnitudes. A dominant WGM in one material might be negligible in another one. Furthermore, due to the vectorial nature of WGMs and the fact that each elastic wave has a specific particle displacement, each WGM vectorial component needs to be studied separately. This point is treated in more detail in the next subsection.

4.1.2. *Radiated elastic waves*

Previous wave sources $\boldsymbol{\sigma}^{tot}$ (for each material) are now used by CIVA-UT to compute the radiated elastic field. In this simulation, the test piece is assumed to be semi-infinite and wave amplitudes are taken below the center of the EMAT at a depth of $z = 75\,\mathrm{mm}$. The time-dependent *z*-displacement waveforms at this point are shown in Fig.10. The first wave packet (with the shortest time of flight $\in [13, 14]\mu s$) corresponds to the fastest wave, *i.e.,* the longitudinal wave (L). As expected, in LCS the dominant Lorentz force (mostly tangential) gives rise to a shear (S) wave amplitude larger than that of the longitudinal L-wave. In nickel, the dominant magnetostriction equivalent force (mostly normal) gives rise to an L-wave amplitude larger than that of the S-wave. For the two intermediate materials (AISI410 and Z20C13) both L and S waves are generated with similar magnitudes. Interestingly the L wave time signature seems to depend on the material, unlike that of the S wave.

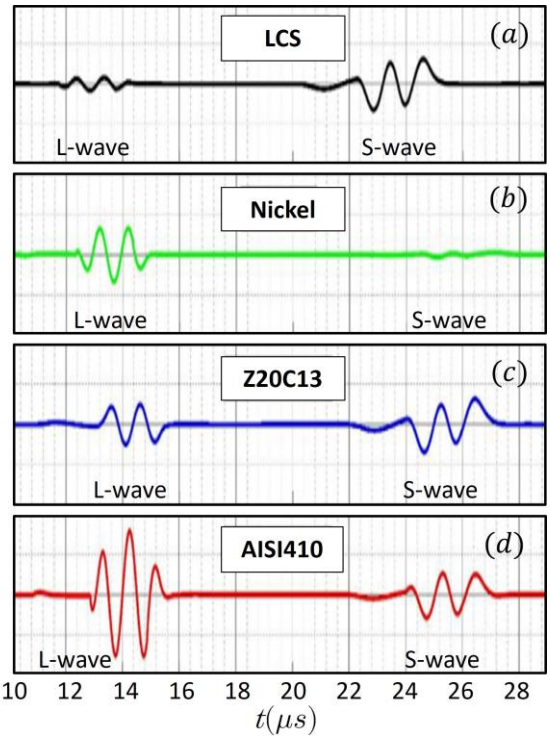

Fig.10. Time-dependent particle displacement L and S waves radiated in the four studied materials. The first packet (with the shortest time of flight $\in [13, 14]\mu s$) corresponds to L wave.

To understand why this is so, one recalls that the latter is generated mostly by a single WGM (Lorentz force), while the former is generated by both magnetic force (bulk and surface) and magnetostriction. Such WGMs do not always have the same spatial distribution and can interact destructively, depending on the material magnetostriction properties.

Field maps (of maximum amplitude of a given quantity) are presented in Fig.11. Due to lack of space, and the intimate correlation between maps and previously studied WGMs spatial distributions, only results of AISI410 are shown. Each WGM and the total distribution were treated separately. Whilst S-wave maps show all WGMs to be dominated by EM force, those for L-wave have contributions of comparable magnitudes. Curiously EM-force treated separately leads to a displacement amplitude (for S) larger than that of $\boldsymbol{\sigma}^{tot}$; this illustrates the fact that WGMs do not always interact constructively. The present result further confirms the assertion that the rule when designing an EMAT or trying to understand EMAT measurements is to evaluate each generation mechanism contribution and compare their respective vectorial components, as each component can give rise to a different wave type.

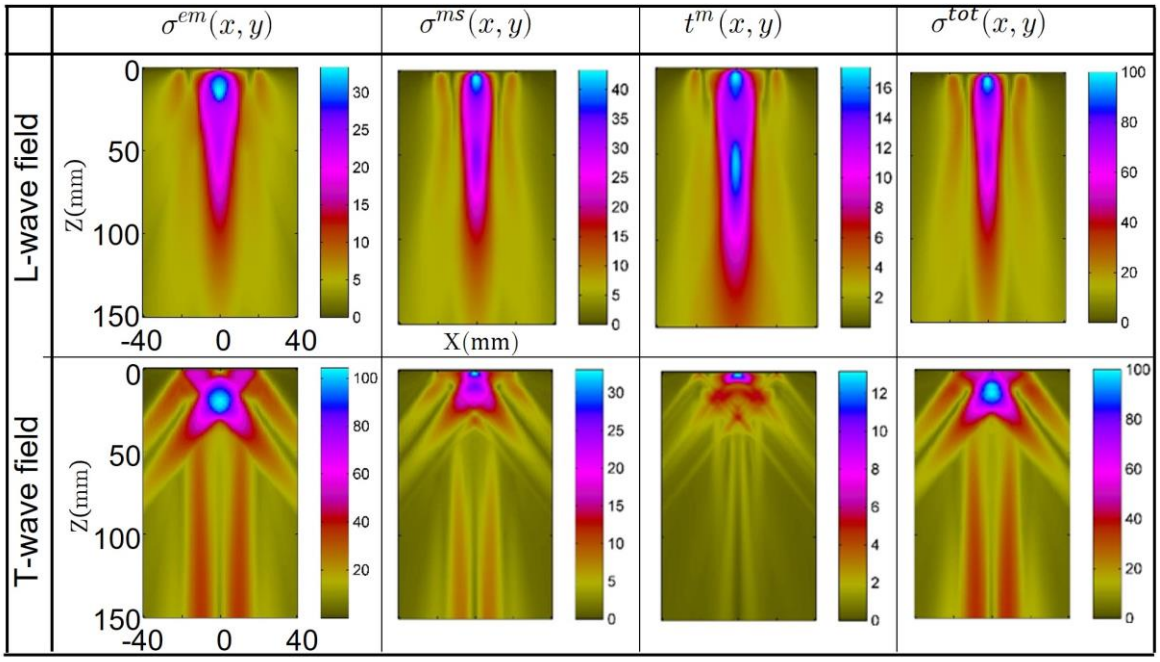

Fig.11. Field maps of L and S waves radiated by the EMAT in AISI410. First to fourth column: $\boldsymbol{\sigma}^{em}, \boldsymbol{\sigma}^{ms}, \boldsymbol{t}^{m}, \boldsymbol{\sigma}^{tot}$.

4.2. Influence of EMAT excitation

In this subsection, we are interested in WGMs as functions of EMAT excitation (I_e and B_{sz}). Given that in the present EMAT configuration, magnetic and magnetostrictive properties manifest themselves mostly through the normal component of WGMs, only this component is considered, for $I_e \in [0;\ 100]$A and $B_{sz} \in [0;\ 4]$T, while the frequency is kept constant and equal to 1 MHz. The normalized maximum amplitude of each WGM is plotted as a function of I_e for LCS in Fig.12a, and as function of B_{sz} for LCS in Fig.12b, for Ni in Fig.12c, and for Z20C13 in Fig.12d. The linear dependency of these maxima on current intensity is expected since the model was developed under the hypothesis of piezomagnetic behavior. Such an assumption is valid even at high intensities, as shown by Fig.2, (for $I_e = 175$ A). This is also the case for the rest of the materials, however, due to the lack of space, only one material is presented here. The normal dynamic magnetic induction is around 100 mT, which is fifteen times smaller than that of the static one. This linear dependency was also observed for the other materials (whose results are not shown). For the material with the weakest magnetic and magnetostrictive properties (LCS), the electromagnetic force – specifically Lorentz force – dominates. Looking now at Fig.12b, one notices that magnetostriction WGM decreases non-linearly with increasing B_{sz}. This is due to the nonlinear magnetostrictive behavior (Fig.8), which shows that for high B_{sz}, magnetostriction saturates, leading to $\boldsymbol{d}^{ms} = \boldsymbol{0}$ (see Eq.4). The divergence at low B_{sz} is due to PMH being invalid in this region. For this material (weak magnetic properties), electromagnetic WGM – specifically Lorentz force – dominates that of magnetic traction. The cases of nickel (Fig.12c) and Z20C13 (Fig.12d) have similar tendencies. The former shows, once again, that high magnetic permeability and electric conductivity do not necessarily lead to strong electromagnetic force, because of the relatively small skin depth. The latter shows that WGMs do not always interact constructively, as evidenced by the dip of $\sigma_z{}^{tot}$ (bellow σ_z^{ms}) at around $B_{sz} = 0.7$ T.

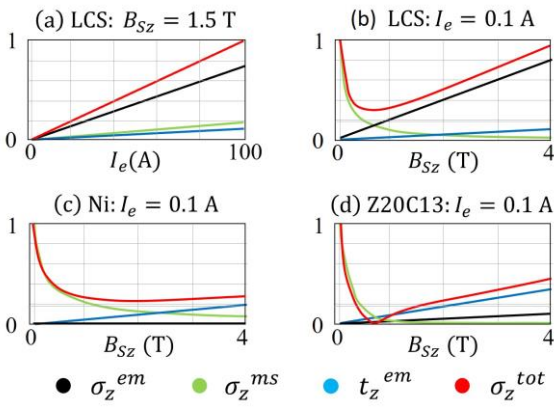

Fig.12. Maximum amplitudes for each WGM for three different materials (LCS, Ni, and Z20C13), as functions of current intensity (a), and static magnetic induction (c) LCS, (d) Ni and (d) Z20C13.

Present results showed that assuming linear magnetic behavior is sufficient to prove the premise of the paper (*i.e.*, wave generation mechanisms depended strongly on material properties and on EMAT excitation). However, this assumption may lead to inaccuracy, as seen in Fig.7 (Sec.3.3), since magnetic behavior is rarely linear. Complementary studies were carried out considering nonlinear behavior. Their conclusion regarding the premise of the present work remains the same as that for linear behavior.

5. Conclusion

A solution to the problem of elastic wave generation (WGP) by EMAT in ferromagnetic materials has been proposed. The tools used include magnetic and magnetostrictive constitutive laws and numerical solvers for both electromagnetic induction and elastic wave radiation problems. The overall method is based on the two fundamental hypotheses of infinitesimal strain and piezomagnetic behavior. Both hypotheses were verified by experiments. The overall model was used to assess the validity of the premise of this paper, that all WGMs (electromagnetic force, magnetostriction strain, and magnetic traction) should be considered when designing an EMAT for applications involving ferromagnetic media, as none is always negligible. To this end, parametric studies were carried out to evaluate WGMs as functions of material properties and EMAT excitation. For a given EMAT, various excitations and four ferromagnetic materials with contrasting electromagnetic properties (nickel, AISI410, Z20C13, and low-carbon steel) were considered. These studies lead to the conclusion that WGMs depend greatly on material properties and EMAT excitation. A combination of material properties and excitation yields a predominant WGM that is negligible for another combination.

The proposed method to solve WGP offers a framework to predict WGMs as functions of material properties, EMAT geometry, and excitation. Such predictions are required in EMAT design for optimal elastic wave radiation in ferromagnetic media. The method is readily usable to deal with pre-stressed ferromagnetic materials, which is the subject of future work.

6. References

[1] R. B. Thompson, J. F. Smith, S. S. Lee, Microstructure-independent acoustoelastic measurement of stress, Appl. Phys. Lett. 44 (1984) 296-298.

[2] A. V. Clark Jr., J. C. Moulder, Residual stress determination in aluminum using electromagnetic acoustic transducers, Ultrasonics 23 (1985) 253-259.

[3] M. Hirao, H. Ogi, H. Fukuoka, Resonance EMAT system for acoustoelastic stress measurement in sheet metals, Rev. Sci. Instrum. 64 (1993) 3198-3205.

[4] M. Kato, T. Sato, and K. Kameyama, Spatial localization of stress-perturbing wave generated by an Electromagnetic Acoustic Transducer, IEEE. Trans. Ultrason. Ferr, Freq. Contr. 44 (1997) 1132-1139.

[5] C. Pei, S. Zhao, T. Liu, Z. Chen, A new method for plastic strain measurement with Rayleigh wave polarization, Ultrasonics 88 (2018) 168-173.

[6] Z. Liu, A. Li, Y. Zhang, L. Deng, B. Wu, C. He, Development of a directional magnetic-concentrator-type electromagnetic acoustic transducer for ultrasonic guided wave inspection, Sensor Actuator A 303 (2020), 111859.

[7] Y. Zhang, Z. Qian, B. Wang, Modes control of Lamb wave in plates using meander-line Electromagnetic Acoustic Transducers, Appl. Sci. 10 (2020) 3491.

[8] R. B. Thompson, Generation of horizontally polarized shear waves in ferromagnetic materials using magnetostrictively coupled meander-coil electromagnetic transducers, Appl. Phys. Lett. 34 (1979) 175-177.

[9] J. He, S. Dixon, S. Hill and K. Xu, A New Electromagnetic Acoustic Transducer design for generating and receiving S0 Lamb waves in ferromagnetic steel plate, Sensors 17 (2017) 1023.

[10] R. B. Thompson, A model for the electromagnetic generation and detection of Rayleigh and Lamb waves, IEEE Trans. Son. Ultrason. 20 (1973) 340-346.

[11] M.R. Gaerttner, W.D. Wallace, and B. W. Maxfield, Phys. Rev. 184, (1969) 702.

[12] L. Vandevelde, J. A. A. Melkebeek, A Survey of magnetic force distributions based on different magnetization models and on the virtual work principle, IEEE Trans. Magn. 37 (2001) 3405-3409.

[13] R. Sanchez-Grandia, V. Aucejo-Galindo, A. Usieto-Galve, R. Vives-Fos, General formulation for magnetic forces in linear materials and permanent magnets, IEEE Trans. Magn. 44 (2008) 2134-2140.

[14] J. R. Melcher, Continuum Electromechanics, (The MIT Press, Cambridge, MA, 1981).

[15] O. Barré, P. Brochet M. Hecquet, Experimental validation of magnetic and electric local force formulations associated to energy principle, IEEE Trans. Magn. 42 (2006) 1475.

[16] R. Sanchez-Grandia, R. Vives-Fos V. Aucejo-Galindo, Magnetostatic Maxwell's tensors in magnetic media applying virtual works method from either energy or co-energy, Eur. Phys. J. Appl. Phys. 35 (2006) 61.

[17] A. Bossavit, Bulk forces and interface forces in assemblies of magnetized pieces of matter, IEEE Trans. Magn, 52 (2016) 229-232.

[18] R. S. Grandía, V. A. Galindo, A. U. Galve, R. V. Fos "General formulation for magnetic forces in linear materials and permanent magnets". IEEE Trans. Magn. 44 (2008) 2134-2140.

[19] M. Seher, P. B. Nagy, On the separation of Lorentz and magnetization forces in the transduction mechanism of Electromagnetic Acoustic Transducers (EMATs), NDT&E Int. 84 (2016) 1-10.

[20] R. Ribichini, F. Cegla, P. B. Nagy, P. Cawley, Quantitative modeling of the transduction of Electromagnetic Acoustic Transducers operating on ferromagnetic media, IEEE Trans. Ultrason. Ferr. Freq. Contr. 57 (2010) 2808-2817.

[21] R. Ribichini, F. Cegla, P. B. Nagy, P. Cawley, Study and comparison of different EMAT configurations for SH wave inspection, IEEE T Ultrason. Ferr, Freq. Contr. 58 (2011) 2571-2581

[22] M. Hirao, H. Ogi, An SH-wave EMAT technique for gas pipeline inspection, NDT&E Int. 32 (1999) 127-132.

[23] R. B. Thompson, Mechanisms of electromagnetic generation and detection of ultrasonic Lamb waves in iron nickel alloy polycrystals, JPN J. Appl. Phys. 48 (1977) 4942-4950.

[24] R. B. Thompson, Physical principles of measurements with EMAT transducers, in Physical Acoustics, vol. 19, New York, Academic Press, p. 157–200, 1990.

[25] E. C. Ashigwuike, O. J. Ushie, R. Mackay, W. Balachandran, A study of the transduction mechanisms of electromagnetic acoustic transducers (EMATs) on pipe steel materials, Sensor Actuator A 229 (2015) 154–165.

[26] L. Daniel, O. Hubert, M. Rekik, A simplified 3D constitutive law for magneto-mechanical behaviour, IEEE Trans. on Magn. 51 (2015) 7300704.

[27] D. C. Jiles, Theory of the magnetomechanical effect, J. Phys. D: Appl. Phys. 28 (1995) 1537.

[28] https://www.extende.com/fr

[29] F. Henrotte, H. V. Sande, G. Deliége, K. Hameyer, Electromagnetic force density in a ferromagnetic material, IEEE Trans. Magn. 40 (2004) 553-556.

[30] B. Clausse, A. Lhémery, Transformation of body force generated by noncontact sources of ultrasound in an isotropic solid of complex shape into equivalent surface stresses, Wave Motion, 60 (2016) 135.

[31] A. Lhémery, A model for the transient ultrasonic field radiated by an arbitrary loading in a solid, J. Acoust. Soc. Am. 96 (1994) 3776.

[32] D. Xiao et al,. "A novel reflection removal method for acoustic emission wave propagation in plate-like structures." Journal of Vibroengineering, Vol. 17, Issue 5, pp. 2322-2337. (2015)

[33] C. Rouge, A. Lhémery, D. Ségur, Transformation of body force localized near the surface of a half-space into equivalent surface stresses, J. Acoust. Soc. Am. 134 (2013) 2639.

[34] L. Daniel, M. Rekik, O. Hubert, A multi-scale model for magneto-elastic behaviour including hysteresis effects, Arch. Appl. Mech. 84 (2014) 1307-1323.

[35] L. Li, Stress effects on ferromagnetic materials: investigation of stainless steel and nickel, PhD, Iowa State University, (2004).

[36] B. Clausse, Modélisation des traducteurs électromagnétiques acoustiques (EMAT) pour le contrôle non-destructif (CND) de milieux ferromagnétiques, PhD, Université Paris Saclay, (2018).

[37] C. Rouge, Modélisation du rayonnement ultrasonore par un traducteur EMAT dans une pièce ferromagnétique, PhD, Université Bordeaux 1, (2013).

[38] M. Hirao, H. Ogi, EMATs for science and industry: noncontacting ultrasonic measurements, (Kluwer Academic Publishers, 2003).

[39] A. Lhémery, An analytic expression for the transient ultrasonic field radiated by a shear wave transducer in solids, J. Acoust. Soc. Am. 96 (1994) 3787-3791.